Preprints of the 21st IFAC World Congress (Virtual)
Berlin, Germany, July 12-17, 2020

Design and control of a prototype structure that adapts to loading through large shape changes

Arka P. Reksowardojo[1]*, Gennaro Senatore[1], Apoorv Srivastava[2], Ian F. C. Smith[1], Henry Unterreiner[3], Chris Carroll[3]

[1]*Swiss Federal Institute of Technology (EPFL),Lausanne, Switzerland, *arka.reksowardojo@epfl.ch*
[2]*Indian Institute of Technology Bombay (IIT Bombay), Mumbai, India*
[3]*Arup UK, Bloomsbury, London, United Kingdom*

Abstract: This paper reports on experimental testing that was carried out on a prototype adaptive structure designed to counteract the effect of loading through controlled large shape changes. The prototype is 6.6 m truss equipped with 12 linear actuators which has been designed through a method that combines geometry optimization and non-linear shape control. The structure is designed to adapt into target shapes that are optimal under each load case. Shape adaptation is achieved through controlled length changes of linear actuators that strategically replace some of the structure elements. The actuator placement is optimized to control the structure into the required target shapes. This way, material utilization is maximized and thus material energy embodied is reduced. Experimental testing is carried out to verify numerical findings and investigate the feasibility of the design method. The applied load is inferred through a classification model based on supervised learning. A control algorithm based on a linear-sequential form of geometry optimization is proposed. Experimental results show that this method successfully allows for real-time shape adaptation to achieve stress homogenization under various loading conditions.

Keywords: adaptive structures, integrated structure-control design, non-linear shape control, embodied energy

1. INTRODUCTION

Civil structures are designed to satisfy strength and deformation criteria for extreme and thus rarely occurring loads. Consequently, the structural capacity is underutilized for most of the structure service life. However, the building sector is globally responsible for 40% of the energy use (European Commission, 2016) and 50% of the material consumption (OECD, 2019), and therefore it has become important to minimize environmental impacts of load-bearing structures.

Smart and adaptive structures that can react to loading through sensing and actuation offer a potential solution to significantly reduce the embodied impacts of load-bearing structures. Adaptive structures are equipped with sensors and actuators to maintain optimal performance through active control against changing loading conditions (Soong, 1988). Structural adaptation has been studied as a means to reduce the structure dynamic response under strong loading events (e.g. earthquakes, strong winds) (Reinhorn, et al., 1993; Soong & Cimellaro, 2009; Wagner, et al., 2018) as well as to improve structural performance by maximizing material utilization (Sobek & Teuffel, 2001; Weidner, et al., 2018). Senatore et al. introduce a new method to design optimal adaptive structures through minimization of the 'whole-life' energy (Senatore, et al., 2019). The whole-life energy comprises an embodied part in the material for extraction, fabrication an construction (Hammond & Jones, 2008) as well as an operational part for structural adaptation. Because actuation is employed to counteract the effect of rarely occurring loads, material embodied energy is significantly reduced at a cost of a small increase in control operational energy (Senatore, et al., 2018a).

Load-bearing capacity can be greatly improved though shape optimization. Shape optimization involves large modifications of nodal positions, to an extent that force distribution can be manipulated significantly (Descamps & Coelho, 2013). However, the geometry obtained through this method cannot adapt and hence structural capacity is not fully utilized under peak loads. Actively controlled large shape changes have been studied for deployable and tensegrity structures (Rhode-Barbarigos, et al., 2012; Sychterz & Smith, 2018). In this context, geometry reconfigurations were achieved through mechanisms based on moving parts. However, this often results in increased weight of the joints and control complexity (Hasse & Campanile, 2009). Shape control of reticular structures, which relies mostly on flexibility, has not been extensively studied theoretically and experimentally. Although shape and force control of an adaptive truss structure has been successfully tested (Senatore, et al., 2018b), geometric nonlinearity was not addressed.

Previous work has shown that a significant stress homogenization can be achieved through controlled large shape changes, such that extreme loads with long return periods are not governing the design (Reksowardojo, et al., 2020). This way, material utilization is maximized. Numerical studies have shown that a significant amount of material embodied energy can be saved with respect to structures that adapt through small shape changes. This paper presents an experimental study on a full-scale prototype adaptive structure designed through the method given in (Reksowardojo, et al., 2020).

2. DESIGN METHOD

The method employed to design the prototype adaptive structure described in the following combines shape optimization with non-linear shape control. Figure 1 shows a flowchart of the design process, which comprises two main stages. Note that the structure used in Figure 1 is shown for illustration purposes only. In stage 1, the objective is minimization of the energy embodied in the material through optimization of element sizing and geometry. The structure is designed to have an optimal shape under each load case. Upon occurrence of a strong loading event, a change of shape takes place to homogenize stresses, and thus material utilization can be maximized since the design is no longer dominated by peak demands.

In stage 2, the actuator placement is optimized so that the structure can be controlled into the target shapes obtained in stage 1. A geometric non-linear force method is employed to obtain

appropriate control commands. It is assumed the structure is subjected to slow varying loads and therefore dynamic effects are not be compensated by active means. In addition, since shape adaptation is only necessary under rarely occurring loads, it is assumed that fatigue is not a critical limit state.

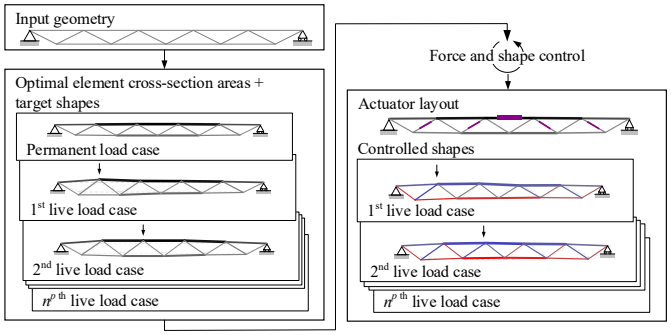

Figure 1. Design method flowchart; element stress is indicated by color shading, blue for compression and red for tension

3. DESCRIPTION OF THE PROTOTYPE

The prototype structure is a 6.6 × 1 × 0.16 m simply supported truss, which comprises 6 bays. The structure is very slender with a span-to-depth ratio of 44/1. It consists of $n^e = 54$ elements connected to $n^n = 20$ nodes. Two nodes at one end are pinned while at the other end two nodes are supported by roller bearings as shown in Figure 2. The structure has a degree of static indeterminacy of 4. All nodes except for the supports (node #1, 7, 8, 14) are controlled.

The structure is designed to support permanent and live load. The permanent load consists of self-weight (SW) and a dead load (DL) which is distributed on the top chord nodes. As shown in Figure 3, there are seven live load (LL) cases. LL1 is a uniformly distributed load applied to the top chord. LL2~LL5 represent a moving load applied in the middle of each bay. LL6 and LL7 are loads applied on each side of the truss in turn thus causing torsion. Load magnitudes are indicated in Figure 3. The structural elements are sized to meet Ultimate Limit State (ULS) requirements under the load cases indicated in Table 1. All elements have a hollow circular section and are made of grade S235JR steel. Element diameter variation is represented by line thickness in Figure 2. Elements #3, 4, 9, 50~54 have a maximum diameter of 42 mm and wall thickness of 1.6 mm. Elements #1, 6, 7, 12, 13~19, 26~49 have a minimum diameter of 22 mm and wall thickness of 1 mm.

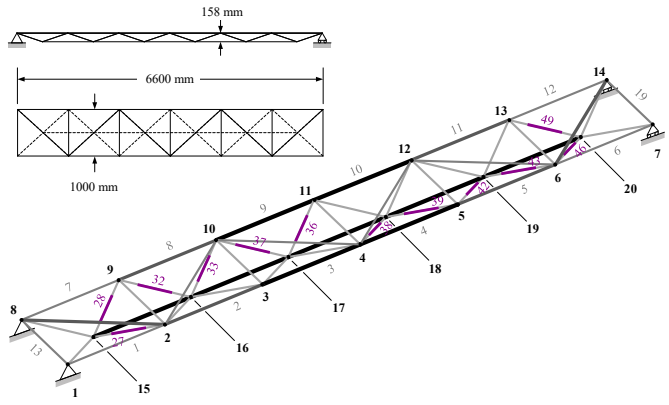

Figure 2. Dimensions, numbering and boundary conditions

Table 1. Load combinations

Load Case	Load combination
LC0	1.35 (SW+DL)
LC1 to LC7	1.35 (SW+DL) + 1.5 (LL1 to LL7)

Since structural adaptation allows to homogenize the stress under strong loading events, material mass (and thus embodied energy) could be reduced by 39% with respect to an equivalent weight-optimized passive structure, which is designed to meet deflection limits set to span/1000 = 6 mm. The structure is built using a MERO modular truss system with ball-type nodes made of grade C45 steel. Due to the high slenderness of the structure, the minimum angle between adjacent elements is 12°. Each tube element is connected to nodes through an M12 bolt which is tighten by means of a hexagonal sleeve.

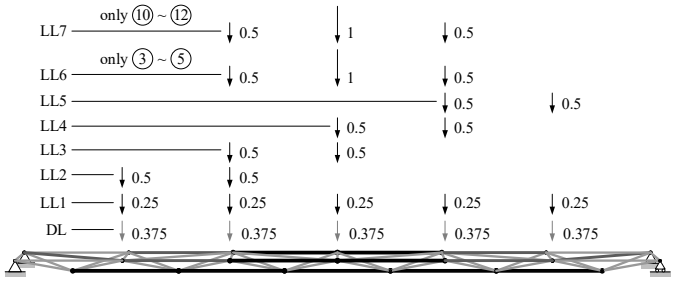

Figure 3. Dead load and live load (kN). The top chord nodes in foreground (#1~#7) and background (#8~#14) are subjected to load unless specified otherwise.

The decking system consists of frames made of four aluminum angle profiles. These frames house acrylic panels that provide a walking surface. The aluminum frames are fixed to the nodes on one side and they are free to slide longitudinally on the other side through a pin-slot mechanism. This way the load is not taken by the decking system which, therefore, does not contribute to the structure stiffness. The supports are designed to be significantly more rigid than the primary structure. Pin-bracket systems constrain the end nodes. At one of the ends, the pin-brackets are mounted on a linear guide rail system.

4. CONTROL SYSTEM

The control system is designed to monitor internal forces and node positions. This information in combination with the actuator stroke-length feedback is processed in real-time to infer location and magnitude of the external load. Geometry optimization is then carried out to compute the target shape under the inferred load. An inverse problem is solved to obtain the actuator commands in order control the structure into the target shape.

All 54 elements are instrumented with strain sensors. For each element, four strain gauges are placed in a full-bridge type III configuration to measure axial strains. The analogue signals from all strain sensors are converted to into digital signals at a rate of 1 kHz. The nodal positions are monitored through an optical tracking system consisting of eight infrared cameras and retro-reflective markers that are attached to the nodes. Through coordinate reconstruction, all node positions are tracked at a rate of 120 Hz within a ±0.025 mm precision.

As mentioned in Section 2, the actuator locations are determined through an optimization process given in (Reksowardojo, et al., 2020). The resulting layout consists of $n^{act} = 12$ actuators fitted

in some of the bracing elements as shown by magenta lines in Figure 2. Actuators are connected via a Controller Area Network (CAN) bus which allows a two-way data transmission between multiple actuators and the control unit using SAE J1939 communication protocol. The CAN bus is capable of transmitting data frames at a rate of 3 kHz. A single frame contains information that includes control commands and stroke positions feedback.

The control unit consists of: an Intel Core i7, 2.60 GHz quad-core processor as the main computational unit; 54-channel data acquisition system for the strain sensors; 8-channel Ethernet switch for the optical tracking; 2-channel CAN interface for the actuators; 4 24V, DC main power converters each supplying three actuators; a 10V, DC auxiliary power converter and electrical circuitries for the actuator emergency-stop system.

5. CONTROL ALGORITHM

5.1. Load inference

The external load applied to the structure has to be known in order to compute the corresponding target shape through optimization. The structure is modelled as a pin-jointed truss. Therefore, each node has 3 degrees of freedom. The number of degrees of freedom is denoted by n^d. There are $n^d = 3 \cdot n^n = 60$. When the shape and the internal forces of the structure are known through data acquisition, the external loads $\mathbf{p} \in \mathbb{R}^{n^d}$ can be inferred through force equilibrium $\mathbf{Af} = \mathbf{p}$, where $\mathbf{A} \in \mathbb{R}^{n^d \times n^e}$ is the equilibrium matrix containing the element cosine directions, which is updated in real-time based on the measured node positions and $\mathbf{f} \in \mathbb{R}^{n^e}$ is the vector of internal forces obtained through the strain sensors. Since the structure undergoes large shape changes, it is important to update **A** based on the measured node positions. Due to non-linear effects caused by joint fixity which is not modelled (the structure is modelled as a pin-jointed truss), the error on the inferred load through force equilibrium is not negligible. For a statically-determinate small-scale prototype (Reksowardojo, et al., 2019), it was sufficient to compensate for the error using a simple linear regression model. However, in this case linear regression was not sufficient to detect accurately location and magnitude of the load. Instead, a classification approach through supervised learning has been implemented. A loading event $\mathbf{p}$ is reduced to a discrete two dimensional metric $\tilde{\mathbf{p}} \in \mathbb{Z}^2$ containing indices that correspond to a predetermined set of load locations (i.e. top chord node positions) as well as load magnitudes. This way $\mathbf{p}$ becomes a vector-scalar product:

$$\mathbf{p} = \mathbf{P}_{\tilde{p}_1} \mu_{\tilde{p}_2}. \tag{1}$$

$\mathbf{P} \in \mathbb{R}^{n^d}$ is a vector containing $0 \le P_k \le 1$ denoting the location of the nodes onto which the load is applied. The scalar μ denotes the magnitude of the applied load. There are 50 load location classes and 3 load magnitude classes (0.8, 1.6 and 2 kN). Classification of the load magnitude was carried out through a model based on support vector machines (SVM). SVM has been successfully employed in a variety of classification applications with small to moderate number of classes (Vapnik, 2013). Since there is a large number of load location classes, classification of the load position was carried out through a model based on a shallow neural network comprising of 2 hidden layers with 50 neurons each. Training the same model using SVM would have been computationally inefficient since it requires a *one-versus-all* approach whereby a binary classifier is trained for each class (Erfani, et al., 2016). The training dataset was collected by applying loads for all location and magnitude classes. For each pair of location and magnitude, the load was fixed and the structure was controlled to the corresponding target shape. Data acquisition was carried out with a sampling frequency of 5 Hz. For the load location classification, the independent variables are the element internal forces and the actuator stroke length feedback. For the load magnitude classification, the independent variables are the internal forces of some select elements to reduce the dimension of the dataset. In total, 153000 observations are collected for the training dataset.

5.2. Computation of target shape

The shape optimization employed in the control algorithm is formulated similarly to that adopted for the design of the structure (Reksowardojo, et al., 2020). However, instead of minimizing the embodied energy (and thus material mass), the objective function (2) in this context is the minimization of the total length change of the elements $\Delta\mathbf{l} \in \mathbb{R}^{n^e}$ subject to constraints that include force equilibrium (3), element stability and admissible stress (4) as well as bounds on the node positions (5) to avoid unfeasible shape changes.

$$\min_{\mathbf{x}} \Delta\mathbf{l}^T \Delta\mathbf{l}, \text{ s.t.,} \tag{2}$$

$$\mathbf{Af}^t = \mathbf{p}, \tag{3}$$

$$f_i^t \le \sigma_i^+ \alpha_i; \quad f_i^t \ge \max\left(\sigma_i^- \alpha_i, -\pi^2 EI_i / l_i^2\right), \tag{4}$$

$$\Delta\mathbf{d}^l \le \Delta\mathbf{d}^t \le \Delta\mathbf{d}^u. \tag{5}$$

The optimization variables are $\mathbf{x} = [\mathbf{f} \quad \Delta\mathbf{d}^t]^T$, where the superscript *t* stands for *target*. $\mathbf{f}^t \in \mathbb{R}^{n^e}$ are the target internal forces in equilibrium (4) with the external load $\mathbf{p}$, which are constrained to avoid element buckling as well as a stress higher than the admissible value (4). E, I, α, σ^- and σ^+ are the Young's modulus, the second moment of area, admissible tensile and compressive stress, respectively. $\Delta\mathbf{d}^t \in \mathbb{R}^{n^d}$ is the difference between the node positions of the shape before control $\mathbf{d}^0 \in \mathbb{R}^{n^d}$ and those of the target shape $\mathbf{d}^t$. The objective function $o(\mathbf{x})$ in (2) can be expanded as:

$$o(\mathbf{x}) = \Delta\mathbf{l}^T \Delta\mathbf{l} = \frac{1}{2} \sum_{i=1}^{n^e} \left(\left\| \mathbf{C}_i \left(\mathbf{d}^0 + \Delta\mathbf{d}^t \right) \right\|_2 - \left\| \mathbf{C}_i \mathbf{d}^{initial} \right\|_2 \right)^2, \tag{6}$$

where $\mathbf{d}^{initial} \in \mathbb{R}^{n^d}$ is the undeformed shape (no applied load). $\mathbf{C}_i \in \mathbb{R}^{n^d \times n^d}$ is the connectivity matrix for the i^{th} element. This matrix contains all zero except for the rows corresponding to the degrees of freedom of the i^{th} element ends which are set to +1 and −1 (Achtziger, 2007). The optimization problem in (2)~(6) is nonlinear and nonconvex, therefore it requires significant computational resources to be solved to local optimality. Since the aim is to employ this method within a real-time control process, linearization has been formulated.

Linearization implies that the shape optimization problem given in (2)~(6) is carried out as series of small shape changes. In each step the operating point $\mathbf{x}^0$ is set to $\mathbf{x}^0 = [\mathbf{f}^0 \quad \mathbf{0}]^T$ where $\mathbf{f}^0$ are the internal forces before a shape update. $\Delta\mathbf{d}^0$ is set to zero because optimization is carried out sequentially by updating the shape $\mathbf{d}^0$

. The objective of this process is to obtain a new point $\mathbf{x} = [\mathbf{f}^t \quad \Delta\mathbf{d}^t]^T$ for next shape update. The equality constraint on force equilibrium (3) and the inequality constraint for element buckling (4) are expressed as explicit functions of the optimization variables:

$$\mathbf{q}(\mathbf{x}) = \mathbf{A}\mathbf{f}^t - \mathbf{p}, \tag{7}$$

$$\mathbf{A} = \begin{bmatrix} \mathbf{A}_i & \cdots & \mathbf{A}_{n^e} \end{bmatrix}, \ \mathbf{A}_i = \sqrt{2}\frac{\mathbf{C}_i\left(\mathbf{d}^0 + \Delta\mathbf{d}^t\right)}{\left\|\mathbf{C}_i\left(\mathbf{d}^0 + \Delta\mathbf{d}^t\right)\right\|_2} \tag{8}$$

and:

$$r_i^{cr}(\mathbf{x}) = -f_i^t + \frac{2\pi^2 EI_i}{\left\|\mathbf{C}_i\left(\mathbf{d}^0 + \Delta\mathbf{d}^t\right)\right\|_2^2}, \ \forall i \in \{1, \cdots, n^e\}. \tag{9}$$

Expanding $o(\mathbf{x})$, $\mathbf{q}(\mathbf{x})$ and $\mathbf{r}^{cr}(\mathbf{x})$ around $\mathbf{x}^0$, the linear approximation of the shape optimization problem is:

$$\min_{\mathbf{x}} \left\{ \mathbf{0} \quad \nabla_{\Delta\mathbf{d}^t} o \Big|_{\Delta\mathbf{d}^t = \mathbf{0}} \right\} \mathbf{x}, \text{ s.t.,} \tag{10}$$

$$\left[\nabla_{\mathbf{f}^t} \mathbf{q} \Big|_{\Delta\mathbf{d}^t = \mathbf{0}} \quad \nabla_{\Delta\mathbf{d}^t} \mathbf{q} \Big|_{\Delta\mathbf{d}^t = \mathbf{0};\ \mathbf{f}^t = \mathbf{f}^0} \right] \mathbf{x} = \mathbf{p}, \tag{11}$$

$$\left[-\mathbf{I} \quad \nabla_{\Delta\mathbf{d}^t} \mathbf{r}^{cr} \Big|_{\Delta\mathbf{d}^t = \mathbf{0}} \right] \mathbf{x} \le \mathbf{f}_{cr} \Big|_{\Delta\mathbf{d}^t = \mathbf{0}}, \tag{12}$$

$$\sigma^- \boldsymbol{\alpha} \le \mathbf{f}^t \le \sigma^+ \boldsymbol{\alpha}, \tag{13}$$

$$\Delta\mathbf{d}^l \le \Delta\mathbf{d}^t \le \Delta\mathbf{d}^u. \tag{14}$$

The computational cost of each iteration is low because the linearized optimization can be solved efficiently using the simplex method.

5.3. Computation of control commands

The control commands $\Delta\mathbf{l}^c \in \mathbb{R}^{n^{act}}$ to cause the change of node positions $\Delta\mathbf{d}^t$ obtained from solving (10)~(14) are computed through constrained least square optimization:

$$\min_{\Delta\mathbf{l}^c} \left\| \mathbf{S}_f \Delta\mathbf{l}^c \right\|_2, \text{ s.t.} \quad \mathbf{S}_d \Delta\mathbf{l}^c = \Delta\mathbf{d}^t. \tag{15}$$

Table 2. Pseudocode of the control algorithm

1	infer load $\mathbf{p}$ through classification
2	set as starting point $\mathbf{d}^0$ and $\mathbf{f}^0$ (the measured state)
3	***while*** true ***do***
4	Estimate target shape change $\Delta\mathbf{d}^t$ through shape optimization in (10)~(14)
5	***if*** the change of the objective function (10) between two successive steps is less than a set tolerance ***then break***
6	compute $\Delta\mathbf{l}^c$ through (15)
7	update $\mathbf{d}^0$ and $\mathbf{f}^0$ based on the inferred load $\mathbf{p}$ and control commands $\Delta\mathbf{l}^c$; $(\mathbf{p}, \Delta\mathbf{l}^c) \rightarrow (\mathbf{f}^0, \mathbf{d}^0)$
8	***end while***

The model in (15) implies a small strain assumption within an iteration. The control commands $\Delta\mathbf{l}^c$ obtained from (15) cause the required change of node positions $\Delta\mathbf{d}^t$ and a minimal change of forces within an iteration. The force $\mathbf{S}_f \in \mathbb{R}^{n^e \times n^{act}}$ and shape $\mathbf{S}_d \in \mathbb{R}^{n^d \times n^{act}}$ influence matrices have been obtained by computing the effect of a unitary length change of each actuator in turn on forces and node positions (Senatore, et al., 2019). Once the control command $\Delta\mathbf{l}^c$ is obtained, a nonlinear geometric force method (Luo & Lu, 2006) is employed to update $\mathbf{f}^0$ and $\mathbf{d}^0$ for next iteration of the shape optimization process. The process is stopped when the change of objective function is smaller than a set tolerance. In this work, the tolerance is set to one, which means that the process stops when the squared sum of all element length changes is equal or less than 1 mm^2. Table 2 gives the pseudocode of the control algorithm.

6. EXPERIMENTAL RESULTS

Experimental testing was carried out to: 1) validate the classification-based load inference model; 2) evaluate the computational performance of the linearized shape optimization model as part of a real-time control process and 3) assess the feasibility of stress homogenization through controlled large-shape changes.

The performance of the classification-based load inference model was evaluated by applying loads for each location and magnitude class. In each case, the load was fixed and the structure was controlled to the target shape. All load locations and magnitudes were tested and data was acquired with a sampling rate of 5 Hz. In total, 11575 observations were generated. Figure 4 is the bar chart plot of the confusion matrix indicating the accuracy of the load location classification. The diagonal values (blue bars) indicate the number of correctly classified observations. The off-diagonal values (red bars) show the number of misclassified observations. In the worst case, 76 observations (0.7% of total) were misclassified. Overall 275 observations were misclassified, which is 2.3% of total observations and thus the load location classification model had a 97.7% accuracy.

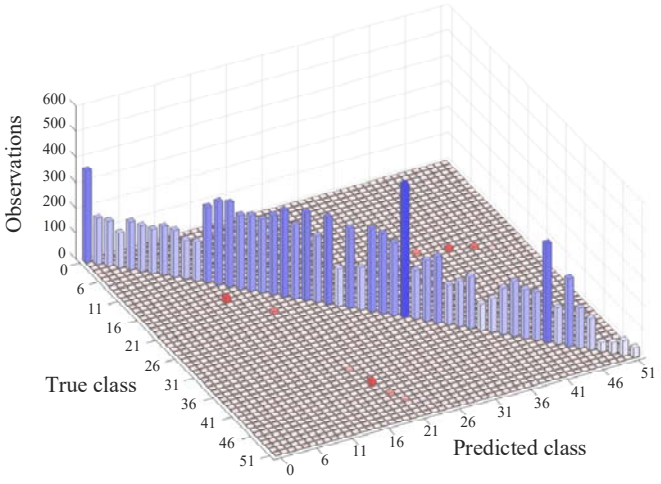

Figure 4. Plot of the confusion matrix showing the accuracy of the load location classification

Table 3 indicate accuracy of the load magnitude classification. In total 161 observations were misclassified, which is 1.4% of the total observations and thus the load magnitude classification model had a 98.6% accuracy.

Table 3. Load magnitude classification accuracy

True class	Predicted class		
	1	2	3
1	3598 (31.1%)	29 (0.3%)	3
2	53 (0.8%)	5384 (46.5%)	42 (0.3%)
3	11	23 (0.2%)	2432 (21%)

The computational efficiency of the linearized shape optimization formulation (10)~(14) was evaluated through a benchmark against the nonlinear formulation (2)~(6). The design load combination cases were considered (Table 1). Nodal positions were measured after shape control, and compared with the target shape computed through the linear shape optimization formulation as well as with the non-linear formulation. For brevity, among all tested load cases (Table 1), only results for LC4 and LC6 are discussed.

The solution of the nonlinear formulation for LC6 took 12 s using sequential quadratic programming (SQP). By providing the analytical Jacobian and Hessian matrices, the same problem took 6 s to solve using the interior point method (IPM). Instead, the sequential-linear shape optimization took only 20 ms. Figure 5 shows the plot of the convergence for the three approaches.

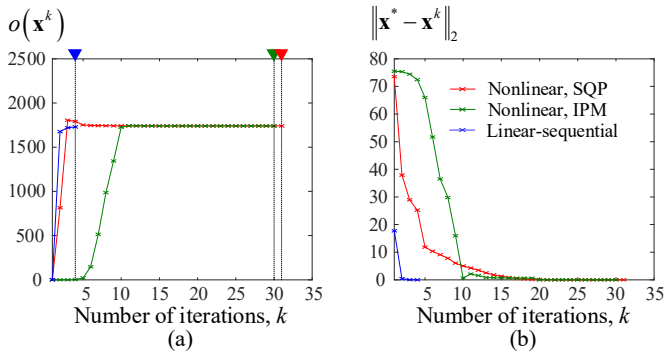

Figure 5. Shape optimization convergence under LC6 in terms of (a) objective function and (b) Euclidean distance with respect to the minimizer

Figure 5a shows the plot of $o(\mathbf{x}^k)$ which is the value of the objective function at the k^{th} iteration. The linear-sequential approach reached convergence faster than the nonlinear approaches. Only four iterations were necessary to reach a minimizer $\mathbf{x}^*$ via the linear-sequential approach. Whereas 31 and 30 iterations were necessary using SQP and IPM, respectively. Figure 5b shows $\|\mathbf{x}^* - \mathbf{x}^k\|_2$, the Euclidean distance between an iterate $\mathbf{x}^k$ and the minimizer $\mathbf{x}^*$. Through inspection of Figure 5a, the value of the objective function using SQP appears to converge after only five iterations. As shown in Figure 5b however, the fifth iteration is still at a significant distance to the minimizer $\mathbf{x}^*$. On the other hand, the second iteration is significantly closer to $\mathbf{x}^*$ through the linear-sequential approach. At the worst case, a full cycle of data acquisition, control algorithm execution, and control command transmission took approximately 30 ms.

The target shapes obtained through the nonlinear approaches (SQP and IPM) are almost identical, the norm difference $\|\Delta\mathbf{d}^{t,SQP} - \Delta\mathbf{d}^{t,IPM}\|_2$ is 1.3×10^{-4} mm. Assuming that $\Delta\mathbf{d}^{t,nonlin} = \Delta\mathbf{d}^{t,SQP} = \Delta\mathbf{d}^{t,IPM}$, Table 4 gives the norm difference between $\Delta\mathbf{d}^{t,nonlin}$ & $\Delta\mathbf{d}^{t,lin}$ and the maximum Euclidean distance between the node positions $\mathbf{d}^{t,nonlin}$ & $\mathbf{d}^{t,lin}$. In addition, Table 4 gives the norm difference and maximum difference between the internal forces $\mathbf{f}^{t,nonlin}$ and $\mathbf{f}^{t,lin}$. The target shapes obtained through linear-sequential approach are very close those obtained through the nonlinear ones. There is a maximum difference of 3.42 mm for node 18 between $\mathbf{d}^{t,nonlin}$ and $\mathbf{d}^{t,lin}$ and 3.55 kN for element 13 between $\mathbf{f}^{t,nonlin}$ and $\mathbf{f}^{t,lin}$ under LC4.

Table 4. Comparison between shape optimization through nonlinear and linear-sequential approach

(a) Nodal positions

Load case	LC4	LC6
$\|\Delta\mathbf{d}^{t,nlin} - \Delta\mathbf{d}^{t,lin}\|_2$ (mm)	8.16	2.94
Max. node distance (mm)	3.42	1.59

(b) Internal forces

Load case	LC4	LC6
$\|\mathbf{f}^{t,nlin} - \mathbf{f}^{t,lin}\|_2$ (kN)	5.39	5.05
Max. difference (kN)	3.55	3.12

The linear-sequential approach was employed in the control algorithm, hence $\Delta\mathbf{d}^t = \Delta\mathbf{d}^{t,lin}$. Table 5 gives the norm difference between the nodes of $\Delta\mathbf{d}^t$ and $\Delta\mathbf{d}^c$ (target shapes and measured controlled shapes) as well as the maximum Euclidean distance between the nodes of $\mathbf{d}^t$ and $\mathbf{d}^c$. Figure 6a and b show the change of shape of the structure loaded by two persons before and after control.

Table 5. Discrepancy between target and controlled shapes

Load case	LC4	LC6
$\|\Delta\mathbf{d}^t - \Delta\mathbf{d}^c\|_2$ (mm)	52.69	40.68
Max. node distance (mm)	19.09	17.17

Figure 7a and b show the bar chart of the element stress before and after shape control – tensile and compressive stress are indicated in red and blue, respectively. A horizontal dashed line indicates the mean. Stress variability is quantified through standard deviation, which is indicated by the width of the shaded band. The maximum mean reduction for tensile and compressive stress is 23% and 22%, respectively (both in LC6). Stress homogenization can be appreciated the most in LC6 since stress variability under shape control is the smallest. There is a significant reduction of the stress for elements 1~12, 29, 47, 51, 52 and 53. The stress for some of the other elements have reversed and increased, namely elements 14~17. The maximum variability reduction for tensile and compressive stress is 24% and 33% respectively in LC6.

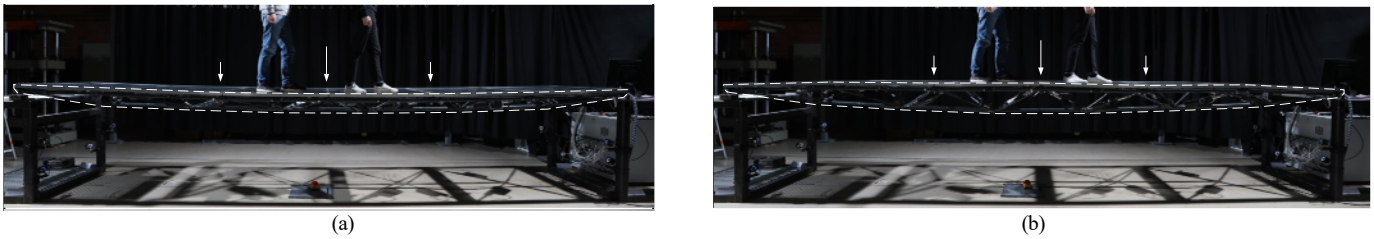

(a) (b)

Figure 6. Shape control LC6: (a) deformed shape, (b) controlled shape

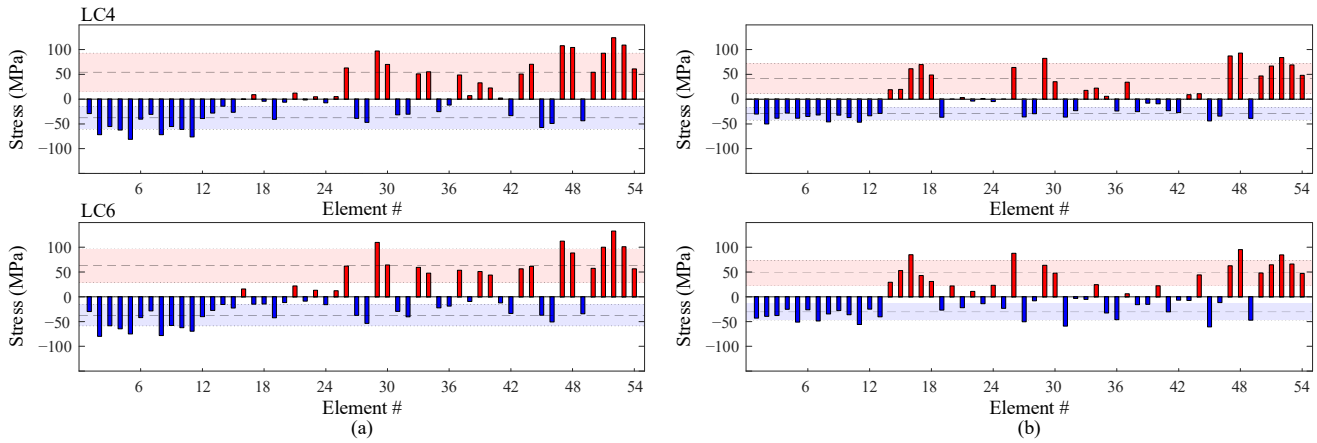

Figure 7. Element stress (a) without and (b) with shape control

7. CONCLUSIONS

The results of this study lead to the following conclusions:

- Accurate detection of the applied load is necessary for structural adaptation. A classification model obtained through supervised learning can be employed to detect the applied load effectively allowing to implement a simple structural model. The structure was modelled as a pin jointed truss; joint fixity has not been taken into account.
- The linearized shape optimization formulation offers a computationally efficient method for real-time control of reticular structures under quasi-static loading. The optimal shapes obtained through the linear-sequential approach are in good accordance with those obtained through nonlinear approaches.
- Experimental study on a large-scale prototype has shown that stress homogenization through large-shape changes is significant. This enables an adaptive structure to operate closer to design limits thus maximizing material utilization and material embodied energy.

Limitations of the method proposed in this paper are:

- The objective of the shape optimization is not based on an explicit minimization of the control energy.
- Considerable discrepancies between target and control shapes are observed.

Future work will look into a reformulation of the method proposed in this paper to minimize the control energy for shape adaptation as well as data-driven compensation to improve control accuracy.

ACKNOWLEDGEMENTS

The authors thankfully acknowledge: Swiss National Science Foundation who provided core funding for this research via project 200021_182033; ARUP Global Research team who provided additional funding through "Global Research Challenge 2018 and MERO Structures.

REFERENCES

Achtziger, W., 2007. On simultaneous optimization of truss geometry and topology. *Structural and Multidisciplinary Optimization,* Volume 33, pp. 285-304.

Descamps, B. & Coelho, R. F., 2013. A lower-bound formulation for the geometry and topology optimization of truss structures under multiple loading. *Structural and Multidisciplinary Optimization,* 48(1), pp. 49-58.

Erfani, S. M., Rajasegarar, S., Karunasekera, S. & Leckie, C., 2016. High-dimensional and large-scale anomaly detection using a linear one-class SVM with deep learning. *Pattern Recognition,* Volume 58, pp. 121-134.

European Commission, 2016. *Study on the Energy Saving Potential of Increasing Resource Efficiency,* Brussels: Directorate-General for Environment.

Hammond, G. & Jones, C., 2008. Embodied energy and carbon in construction materials. *Proceedings of the Institution of Civil Engineers - Energy,* 161(2), pp. 87-98.

Hasse, A. & Campanile, F., 2009. Design of compliant mechanisms with selective compliance. *Smart Materials and Structures,* 18(11), pp. 1-10.

Luo, Y. & Lu, J., 2006. Geometrically non-linear force method for assemblies with infinitesimal mechanisms. *Computers & Structures,* Volume 84, pp. 2194-2199.

OECD, 2019. *Global Material Resources Outlook to 2060, Economic Drivers and Environmental Consequences,* Paris: OECD Publishing.

Reinhorn, A., Soong, T. R. M. & Lin, R., 1993. Full-Scale Implementation of Active Control. II: Installation and Performance. *Journal of Structural Engineering,* 119(6), pp. 1935-1960.

Reksowardojo, A. P., Senatore, G. & Smith, I. F. C., 2019. Experimental Testing of a Small-Scale Truss Beam That Adapts to Loads Through Large Shape Changes. *Frontiers in Built Environment,* Volume 5, p. 93.

Reksowardojo, A. P., Senatore, G. & Smith, I. F. C., 2020. Design of structures that adapt to loads through large shape changes. *The Journal of Structural Engineering (ASCE),* 146(5), p. 04020068.

Rhode-Barbarigos, L. et al., 2012. Mechanism-Based Approach for the Deployment of a Tensegrity-Ring Module. *Journal of Structural Engineering,* 138(4), pp. 539-548.

Senatore, G., Duffour, P. & Winslow, P., 2018a. Energy and Cost Analysis of Adaptive Structures: Case Studies. *Journal of Structural Engineering,* 144(8), p. 04018107.

Senatore, G., Duffour, P. & Winslow, P., 2019. Synthesis of Minimum Energy Adaptive Structures. *Structural and Multidisciplinary Optimization,* 60(3), pp. 849-877.

Senatore, G., Duffour, P., Winslow, P. & Wise, C., 2018b. Shape control and whole-life energy assessment of an 'infinitely stiff' prototype adaptive structure. *Smart Materials and Structures,* 27(1), p. 015022.

Sobek, W. & Teuffel, P., 2001. *Adaptive Systems in Architecture and Structural Engineering.* Newport Beach, CA, United States, SPIE, p. Vol. 4330 (2001).

Soong, T. T., 1988. Active structural Control in Civil Engineering. *Engineering Structures,* 10(4), pp. 74-84.

Soong, T. T. & Cimellaro, G. P., 2009. Future directions in structural control. *Structural Control and Health Monitoring,* 16(7), pp. 7-16.

Sychterz, A. C. & Smith, I. F. C., 2018. Deployment and Shape Change of a Tensegrity Structure Using Path-Planning and Feedback Control. *Frontiers in Built Envioronment,* Volume 4.

Vapnik, V., 2013. *The nature of Statistical Learning Theory.* New York: Springer.

Wagner, J. L. et al., 2018. On steady-state disturbance compensability for actuator placement in adaptive structures. *Automatisierungstechnik,* 66(8), pp. 591-603.

Weidner, S. et al., 2018. The implementation of adaptive elements into an experimental high-rise building. *Steel Construction: Design and Research,* 11(2), pp. 109-117.